Nano Research

Open Access

Research Article

$Ti_3C_2T_x$/liquid metal/Ni chain composites for microwave-Terahertz compatible stealth

Haoran Cheng[1,3], Jiajun Lian[1], Xukai Jiao[1], Yidan Yang[1], Mao Chen[2,3]✉, and Bingbing Fan[2]✉

[1] College of Materials Science and Engineering, National Engineering Research Center for Advanced Polymer Processing Technology, Zhengzhou University, Zhengzhou 450002, China
[2] School of Materials Science and Engineering, Zhengzhou University, Zhengzhou 450001, China
[3] Luoyang Industrial Technology Institute, Zhengzhou University, Luoyang 471100, China

Cite this article: *Nano Research*, **2026**, *19*, 94908596. https://doi.org/10.26599/NR.2026.94908596

ABSTRACT: Achieving compatible electromagnetic (EM) defense across both microwave and Terahertz (THz) regimes remains a formidable challenge in the development of advanced stealth materials. Herein, a novel MXene/liquid metal (LM)/Ni chain composite is strategically engineered through an interfacial synergy modulation and one-dimensional (1D) magnetic structure induction strategy, enabling high-efficiency co-attenuation across the microwave-THz spectrum. This architecture synergistically combines the conductive network of MXene, LM-induced interfacial polarization, and the magnetic loss from Ni chains to achieve superior impedance matching. Remarkably, with a mere 5 wt.% filler loading, the composite achieves a record-low reflection loss (RL_{min}) of −63.1 dB and an effective absorption bandwidth (EAB) of 6.72 GHz. Simulation results further validate its immense potential for radar stealth applications in both civil and military coatings. When fabricated into flexible films, the material demonstrates exceptional EM attenuation in the 0.1–1.6 THz band, yielding a shielding effectiveness (SE) and absorption efficiency of 69.6 and 68.1dB, respectively. Mechanism analysis reveals that the multiscale conductive network, pronounced interfacial polarization, and magneto-dielectric synergistic loss collaboratively facilitate high-efficiency energy dissipation across multiple frequency bands. This work provides a novel design strategy for the development of lightweight, ultra-thin, and ultra-broadband microwave-THz absorption/shielding materials.

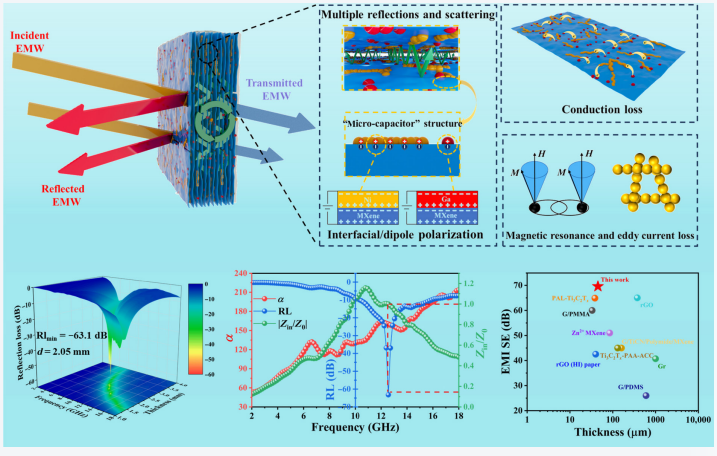

KEYWORDS: $Ti_3C_2T_x$ MXene, microwave absorption, Terahertz shielding, multi-polarization losses, composite films

1 Introduction

The rapid evolution of high-speed communication technologies is driving the continuous expansion of operational frequency bands toward multi-polarization and ultra-wideband regimes [1, 2]. For instance, 5G communication protocols have already occupied the 3.4–3.6 and 24–100 GHz spectra, while nascent 6G technology further penetrates the Terahertz (THz) and even visible light domains [3–5]. Consequently, the communication spectrum now bridges the gap between microwave and THz frequencies, exhibiting significant interdisciplinary and multi-physical characteristics. This paradigm shift inevitably triggers multi-band electromagnetic (EM) leakage and EM interference, posing severe challenges to the operational stability of electronic devices and information security. Simultaneously, the synergistic operation of integrated systems has become a defining feature of modern equipment, where microwave and THz multi-frequency devices frequently coexist within the same operational scenario. Therefore, the development of integrated, multi-band shielding and defense material systems is of paramount strategic significance. Such materials are essential for ensuring security and countermeasures within complex EM environments, particularly in sensitive military

Received: January 19, 2026; **Revised:** February 4, 2026
Accepted: February 23, 2026

✉Address correspondence to Bingbing Fan, fanbingbing@zzu.edu.cn; Mao Chen, mchen@zzu.edu.cn

facilities such as EM shelters, command centers, ammunition depots, and hangars.

Despite significant progress, state-of-the-art defense materials remain predominantly effective within a single frequency band [6, 7] (e.g., microwave). While a limited number of materials have achieved dual-band protection [8, 9] (e.g., microwave/infrared), those capable of compatible microwave and THz wave defense remain remarkably scarce, making it difficult to counter emerging threats from the rapid maturation of THz technologies. More fundamentally, while microwaves are governed by EM theories and infrared/visible light reside in the optical regime, THz waves uniquely bridge the gap between these two domains. This duality presents a formidable challenge in achieving integrated EM-optical defense, as it necessitates the reconciliation of divergent material response mechanisms and the management of complex structural synergies. Consequently, engineering a compatible microwave-THz defense system remains a critical scientific and engineering bottleneck that demands immediate breakthroughs.

The synergistic regulation of material selection and structural design is recognized as an effective avenue for achieving multispectral compatible defense. An ideal material system should exhibit high response and high loss characteristics across diverse wavebands, specifically demonstrating significant dielectric, magnetic, and synergistic losses for both microwave and THz radiations [10, 11]. Simultaneously, rational architectural designs-such as metamaterials [12], topological patterns [13], heterogeneous stacking [14], and three-dimensional (3D) porous networks [15] can further bolster the robustness of wave-matter interactions. For instance, Li et al. [16] developed a digital camouflage strategy spanning the visible to microwave regimes, by simulating high-precision vegetation spectra and multi-level patterns, they realized ultra-broadband EM regulation covering 80% of atmospheric windows and multispectral background matching. Wang et al. [17] inspired by black butterflies, constructed MXene/CMC aerogels with disordered micropores via ice-templating, achieving ultra-broadband THz shielding (70.32 dB) and omnidirectional infrared (IR) stealth through resonant cavity effects. Cheng et al. [18] fabricated hierarchical porous rGO/GONR aerogels via a pyrolysis-reduction process, leveraging optimized impedance matching and low thermal conductivity (< 0.06 W/(m·K)), they integrated high-performance microwave absorption (−63.5 dB) with efficient thermal-insulating IR stealth. Peng et al. [19] engineered core–shell AgNW@C aerogels utilizing one-dimensional (1D) coaxial nanocable networks and 3D porous structures to achieve cross-band compatibility for microwave absorption (−66.5 dB), THz shielding (> 50 dB), and low IR emissivity (0.28). Existing research has shown that the coupling of multi-functional materials with tailored structures can realize multispectral protection across microwave/infrared, microwave/THz, and microwave/infrared/visible light regimes. These advancements verify that the strategy of synergistically engineering material selection and structural design is highly feasible and holds great promise for the development of integrated microwave/THz compatible defense systems.

Among various candidate materials, MXene has been extensively utilized for EM absorption and shielding due to its low density, high specific surface area, tunable surface chemistry, and superior electrical properties [20–22]. LM, with its unique fluidic nature, high metallic conductivity, and the spontaneous formation of a native ultra-thin oxide layer (Ga_2O_3), exhibits significant advantages in EM modulation by inducing intense interfacial polarization [23, 24]. Meanwhile, Ni chains leverage their induced robust magneto-dielectric synergistic effects, playing a pivotal role in optimizing impedance matching and constructing high-performance EM loss networks [25–27]. Furthermore, the lamellar architecture of the thin film facilitates a highly stable attenuation network characterized by optimized impedance matching and abundant polarization sites [28]. This structure not only significantly extends the EM attenuation path and enhances multiple reflections but also achieves high-efficiency, broadband absorption spanning from microwave to THz frequencies within an ultra-thin profile [29, 30].

In this work, a synergistic strategy integrating component optimization (MXene, LM, and Ni chains) with a hierarchical lamellar heterostructure was proposed to develop a novel MXene/LM/Ni composite film for compatible microwave-THz EM defense. Within this multi-dimensional system, two-dimensional (2D) MXene provides robust conductive loss, zero-dimensional (0D) LM nanospheres enhance high-frequency responsiveness by inducing intense interfacial polarization, and the introduction of 1D Ni chains effectively optimizes impedance matching while establishing abundant magnetic loss sites. Benefiting from the structural reinforcement of multiple reflections, scattering, and synergistic polarization attenuation mechanisms inherent in the lamellar architecture, the film achieves a remarkable RL_{min} of −63.1 dB at 12.56 GHz. In the THz regime, it exhibits a superior SE of 69.6 dB with a reflectivity of less than 5%. Simulation analysis demonstrates that the material significantly reduces the radar cross-section (RCS) of targets, showcasing exceptional cross-spectrum stealth performance.

2 Results and discussion

2.1 Characterization of structure and morphology

Figure 1 provides a comprehensive illustration of the modular fabrication process for the MXene/LM/Ni composite films. Initially, few-layered $Ti_3C_2T_x$ MXene nanosheets are synthesized from MAX phase precursors via selective etching followed by liquid-phase exfoliation. Attributed to their ultra-high specific surface area, exceptional mechanical robustness, and high metallic conductivity, the MXene nanosheets serve as both the structural backbone and the primary channels for efficient EM attenuation. Subsequently, gallium-based LM is mechanically fragmented into micro-to-nano scale droplets using probe sonication. The native nano-oxide shell (Ga_2O_3) spontaneously formed on the LM surface enables strong coupling with the hydroxyl (–OH) or fluorine (–F) terminal groups of MXene through hydrogen bonding or Van der Waals interactions, facilitating dense interlayer integration without additional binders. Concurrently, an electrostatic self-assembly strategy is employed, where cationic polyelectrolyte (PDDA)-functionalized Ni chains (positively charged) are meticulously mixed with negatively charged MXene nanosheets in an aqueous medium. The intense electrostatic attraction ensures the uniform anchoring of 1D Ni chains onto the 2D MXene surfaces, effectively suppressing magnetic particle agglomeration and establishing the foundation for magneto-dielectric synergistic units. Finally, the programmed assembly into a layered MXene/LM/Ni composite film with highly ordered heterogeneous interfaces is achieved via vacuum-assisted filtration. In summary, this collaborative design

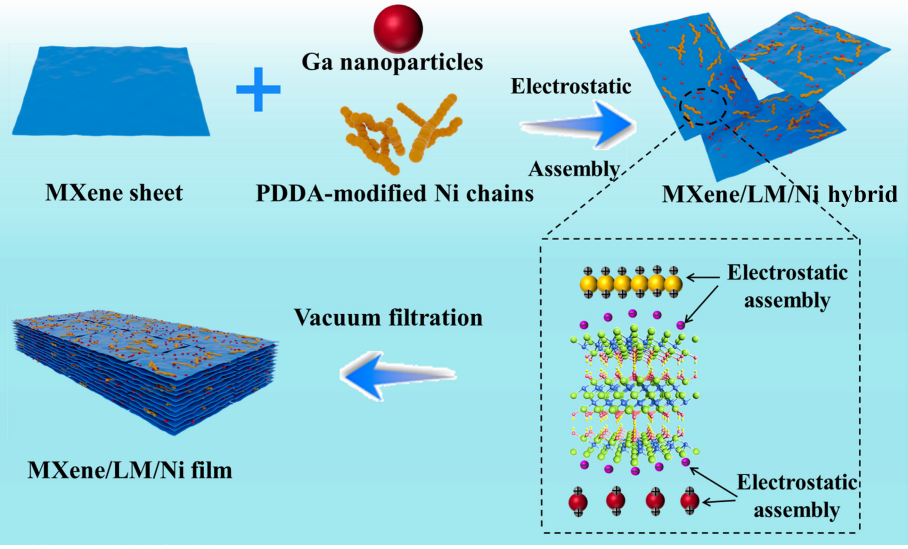

Figure 1 Schematic of the fabrication process for the MXene/LM/Ni composite.

strategy leverages the superior dielectric loss of MXene, the enhanced interfacial polarization and mechanical flexibility afforded by the fluidic LM, and the significant improvements in impedance matching provided by the magnetic Ni chains. The organic integration of these multi-dimensional components within a layered network enables the MXene/LM/Ni films to exhibit exceptional microwave-THz absorption and comprehensive EM defense potential at an ultra-thin profile.

Systematic characterization of the surface and cross-sectional morphologies of the components and the resulting composite films was conducted using scanning electron microscopy (SEM) and transmission electron microscopy (TEM). As shown in Fig. 2(a), the MXene nanosheets exhibit ultrathin and nearly transparent features, confirming the successful exfoliation of few-layered $Ti_3C_2T_x$. Upon sonication, the LM forms spherical micro-nanoscale droplets with a uniform diameter distribution (Fig. 2(b)), whose native oxide shell facilitates stable dispersion within the 2D matrix [31]. Simultaneously, the Ni chains display a characteristic 1D high-aspect-ratio morphology with lengths extending several tens of micrometers (Fig. 2(c)), after functionalization with the cationic surfactant PDDA, they possess a positive surface charge (Fig. S1 in the Electronic Supplementary Material (ESM)). Driven by synergistic electrostatic attraction and Van der Waals forces, the negatively charged MXene nanosheets intimately intertwine with the positively charged Ni chains and LM droplets. It can be clearly observed that the LM droplets are uniformly embedded within the MXene interlayers (Fig. 2(d)), while the Ni chains are effectively encapsulated by the MXene nanosheets (Fig. 2(e)). The anchoring of 0D LM and 1D Ni chains onto the 2D MXene substrate (Fig. 2(f)) constructs a multi-dimensional, continuous hybrid network with abundant heterogeneous interfaces. High-resolution TEM (HRTEM) analysis further reveals distinct lattice fringes in the Ni chain regions with a spacing of 0.2021 nm, corresponding to the (111) crystalline plane of metallic Ni and confirming its high crystallinity [32, 33] (Fig. 2(g)). Figures 2(h) and 2(i) verify the successful construction of the layered MXene/LM/Ni films. The final composite films possess a controlled thickness of 45 μm, and their ultra-thin, lightweight characteristics exhibit immense potential for load-sensitive EM defense applications in flexible electronics.

Multi-dimensional composition and structural characterizations of MXene, MXene/LM, and MXene/LM/Ni composite films were conducted to elucidate the structural evolution, chemical states, and their respective contributions to EM performance. As shown in the XRD patterns (Fig. 3(a)), the pure MXene film exhibits an intense characteristic (002) diffraction peak at approximately 7.4°, corresponding to its typical lamellar structure [34, 35]. This (002) peak is well-preserved in the MXene/LM and MXene/LM/Ni composite films, confirming the structural stability of the 2D MXene skeleton during the hybridization process [36, 37]. However, the peak positions slightly shift toward lower angles, indicating an effective expansion of the interlayer spacing (*d*-spacing) induced by the intercalation of LM nanospheres and Ni chains, which facilitates multiple reflections of EM waves between the layers. In the MXene/LM/Ni pattern, distinct diffraction peaks at 44°, 51.8°, and 76.4° correspond to the (111), (200), and (220) crystalline planes of face-centered cubic (FCC) metallic nickel (PDF #04-0850) [38, 39]. For the LM component, a diffuse broad peak appears between 30° and 40°, attributed to its fluidic state at room temperature. Furthermore, the FT-IR spectra (Fig. 3(b)) reflect the evolution of surface functional groups during composite formation. Pure MXene shows characteristic absorption bands at 3440 cm^{-1} (–OH)、 1630 cm^{-1} (O–Ti), and 580 cm^{-1} (C–F) [40]. In the MXene/LM and MXene/LM/Ni systems, the intensity of the –OH peak significantly decreases, suggesting the formation of strong hydrogen bonding or electrostatic interactions between the oxide layer on the LM surface/Ni chain modifiers and the MXene functional groups [41, 42]. These abundant polar groups are instrumental in modulating dipolar polarization.

The magnetic properties of the composites were characterized via vibrating sample magnetometry (VSM) (Fig. 3(c)). Both the Ni chains and the resulting MXene/LM/Ni composite exhibit distinct ferromagnetic behavior. The saturation magnetization (M_s) decreased from 49.6 emu/g for the pristine Ni chains to 19.5 emu/g for the MXene/LM/Ni film, which is ascribed to the mass dilution effect of the non-magnetic MXene and LM components. Notably, this moderate magnetic response is crucial for achieving optimized impedance matching, as the integration of magnetic loss components mitigates the inherent impedance mismatch typical of highly conductive MXene-based systems, thereby enhancing the

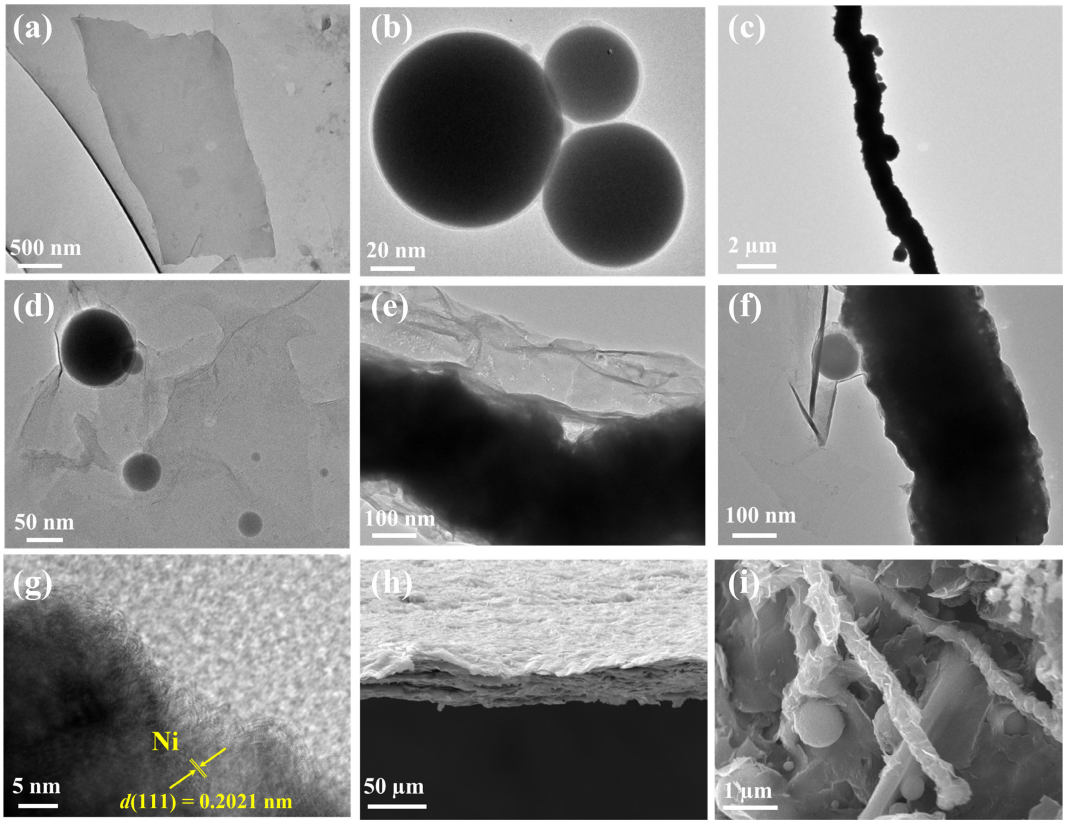

Figure 2 Structural characterization of the MXene/LM/Ni composite. TEM images of (a) MXene, (b) LM, (c) Ni chain, (d) MXene/LM, (e) MXene/Ni chain, and (f) MXene/LM/Ni. (g) HRTEM image of MXene/LM/Ni. (h) The cross-section and (i) surface SEM images of MXene/LM/Ni composite film.

overall microwave and THz absorption performance [43].

The XPS survey spectrum (Fig. 3(d)) clearly identifies the characteristic peaks of Ti, C, O, F, Ga, and Ni, confirming the successful ternary hybridization without discernible impurities. In the high-resolution C 1s spectrum, apart from the C–C bond at 284.8 eV, distinct peaks at 281.9 eV (C–Ti) and 286.1 eV (C–N) are observed (Fig. 3(e)). The latter originates from the PDDA modification on the Ni chain surfaces, signifying robust coupling between the organic and inorganic components. Regarding the O 1s spectrum (Fig. 3(f)), sub-peaks at 532.5 and 530.8 eV, assigned to C–Ti–$(OH)_x$ and O–Ga(III), respectively, further validate the coexistence of MXene and LM at the interface. The Ti 2p spectrum of the MXene/LM/Ni composite exhibits four characteristic peaks at 465.2, 461.9, 459.4, and 456.1 eV, corresponding to Ti–O $2p_{1/2}$, C–Ti–T_x $2p_{1/2}$, Ti–O $2p_{3/2}$, and C–Ti–T_x $2p_{3/2}$ bonds, respectively (Fig. 3(g)). The Ga 2p spectrum is pivotal for identifying the chemical state of LM. The intense peaks at 1117.4 and 1144.6 eV correspond to Ga^{3+} $2p_{3/2}$ and Ga^{3+} $2p_{1/2}$, respectively. Through precise fitting, these peaks are resolved into a metallic Ga^0 peak (approx 1116.9 eV) and an oxidized Ga^{3+} peak (approx 1118.2 eV), indicating that the LM droplets are encapsulated by a native Ga_2O_3 layer (Fig. 3(h)). Finally, the main peaks of the Ni 2p spectrum are located at 873.9 and 855.8 eV, corresponding to Ni $2p_{1/2}$ and Ni $2p_{3/2}$, respectively (Fig. 3(i)), confirming the successful integration of the Ni chains.

2.2 Broadband and strong microwave absorption

EM parameters are fundamental indicators that dictate the microwave absorption performance of composite materials. As a superior conductor, pristine MXene possesses high electrical conductivity and elevated real (ε') and imaginary (ε'') parts of permittivity (Fig. S2(a) in the ESM). However, these characteristics typically result in poor impedance matching, which induces strong secondary reflections of EM waves and subsequently degrades MA performance. In contrast, the ε' values of MXene/LM (Fig. S2(b) in the ESM) and MXene/LM/Ni composites exhibit a more pronounced decline across the measured frequency range compared to pure MXene (Figs. S3(a) and S3(b) in the ESM). It is noteworthy that excessive ε' often leads to impedance mismatch, the 8 wt.% MXene/LM/Ni absorber displays the highest ε' and ε'' values due to the enhanced conductivity network formed by the increased MXene content. The electrostatic self-assembly of LM and Ni chains creates prolific heterogeneous interfaces, both of which trigger intense dipole and interfacial polarization. Furthermore, the distinct resonance peaks in the dielectric loss tangent (tanε) suggest the presence of polarization relaxation processes (Fig. S3(c) in the ESM). These processes can be further elucidated through Cole–Cole semicircles derived from Debye theory. The discernible distorted arcs observed in MXene/LM/Ni composites with varying loadings signify the occurrence of multiple relaxation behaviors (Figs. S4(a)–S4(c) in the ESM). Such enhanced relaxation is primarily ascribed to internal defects and the abundant heterojunctions, which induce significant dipole and interfacial polarization, thereby strengthening the EM wave attenuation capacity [44, 45].

Magnetic loss constitutes another indispensable channel for EM energy dissipation. The real part (μ'), imaginary part (μ''), and magnetic loss tangent ($\tan\delta_\mu$) of the MXene/LM/Ni composites exhibit discernible fluctuations across the measured frequency range, evidencing the presence of active magnetic loss mechanisms

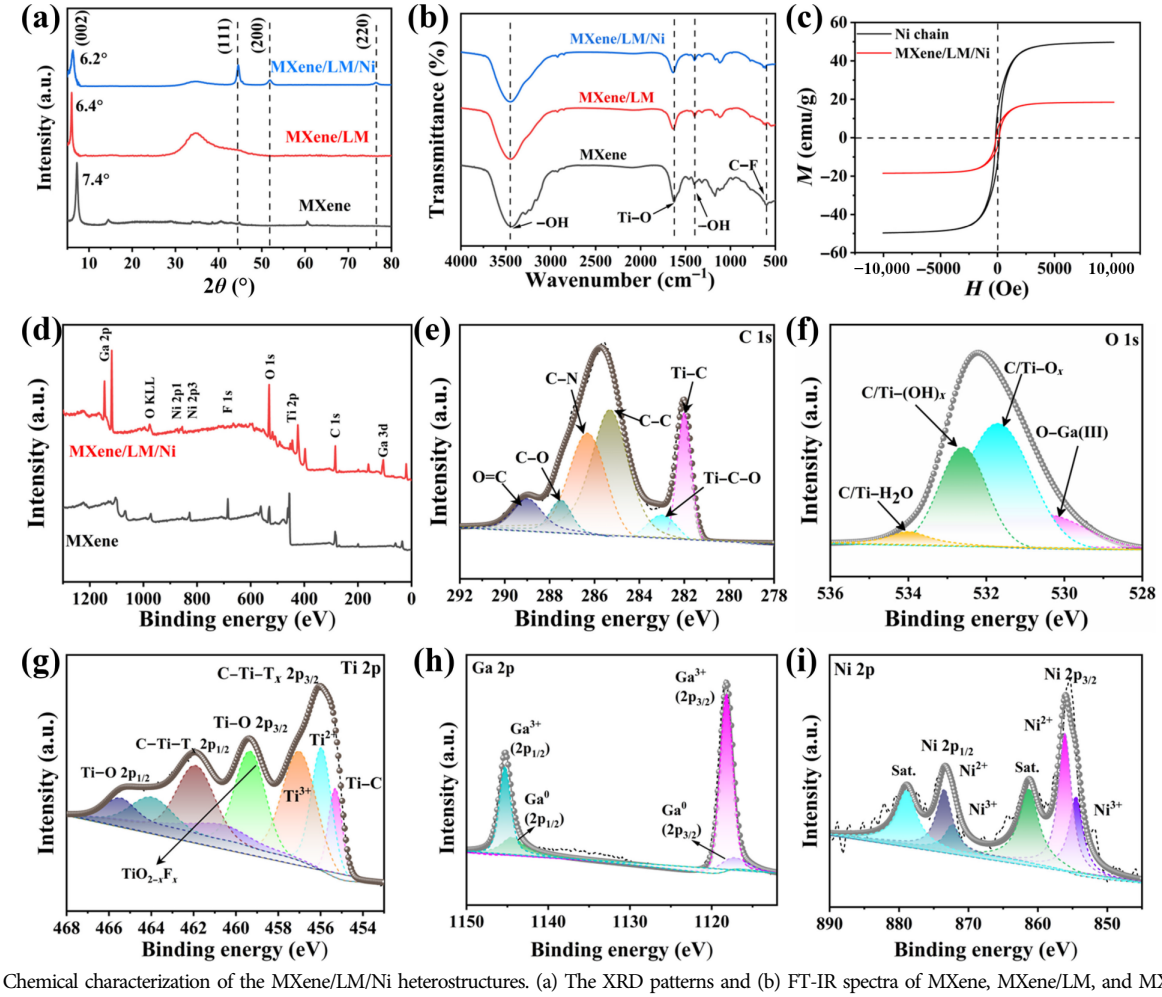

Figure 3 Chemical characterization of the MXene/LM/Ni heterostructures. (a) The XRD patterns and (b) FT-IR spectra of MXene, MXene/LM, and MXene/LM/Ni hybrid. (c) The VSM of MXene/LM/Ni hybrid. (d) The XPS spectra of MXene and MXene/LM/Ni: (e) C 1s, (f) O 1s, (g) Ti 2p, (h) Ga 2p, and (i) Ni 2p.

(Figs. S3(d)–S3(f) in the ESM). To quantify the contribution of eddy current effects, the C_0 parameter was calculated using the formula $C_0 = \mu''(\mu')^{-2}f^{-1}$ to analyze the impact of eddy current loss on the overall magnetic dissipation [46]. The C_0 values for all three samples undergo a notable decline within the 2–7 GHz range and exhibit slight fluctuations across the 7–18 GHz band. These trends suggest that eddy current loss plays a significant role in the magnetic energy attenuation at higher frequencies (Fig. S5 in the ESM).

To comprehensively evaluate the microwave absorption (MA) performance of the MXene/LM/Ni composites in the gigahertz range, the influence of filler loadings (3 wt.%, 5 wt.%, and 8 wt.%) on EM parameters and RL was scrutinized. The RL curves, calculated based on transmission line theory (Fig. 4), clearly demonstrate the superlative tunable MA capacity of the materials across 2–18 GHz. All composite samples outperform pristine MXene in terms of EM attenuation (Fig. S6 in the ESM). At a lower loading of 3 wt.%, the sample achieves a minimum RL_{min} of −20.06 dB at 11.28 GHz (3.65 mm), with an EAB of 5.76 GHz, suggesting the initial formation of an effective EM loss network. As the loading increases to 5 wt.%, the MXene/LM/Ni composite exhibits exceptional MA potential, at a matching thickness of only 2.05 mm, it attains an ultra-low RL_{min} of −63.1 dB, representing near-perfect absorption. Notably, at an even thinner profile of 1.8 mm, the EAB further extends to 6.72 GHz (covering 11.28–18 GHz), highlighting its "thin-and-wide" absorption characteristics. However, at 8 wt.%, the RL_{min} rises to −23.21 dB and the EAB contracts to 5.28 GHz. This degradation is attributed to severe impedance mismatch caused by excessive conductivity, which induces strong surface reflections. Furthermore, the migration of RL peaks toward lower frequencies with increasing thickness is well-explained by the quarter-wavelength ($\lambda/4$) resonance theory [47, 48]. The consistency between the experimental and calculated matching thicknesses confirms the validity of the $\lambda/4$ model (Fig. S7 in the ESM). These findings identify the 5 wt.% MXene/LM/Ni composite as a highly promising candidate for advanced EM wave absorption applications.

To gain deeper insights into the EM loss mechanisms of these complex architectures, the attenuation constant (α) was employed to quantitatively evaluate the dissipation capacity of the absorbers. As depicted in Fig. S8(a) in the ESM, the α values increase monotonically with the MXene/LM/Ni loading, which is primarily ascribed to the enhanced conductivity provided by the increased MXene content. However, the synergy between a moderate α and optimized impedance matching is a prerequisite for achieving high-performance MA. The normalized input impedance (Z_{in}/Z_0) values for various loadings were compared, optimal impedance matching is realized when the Z value approaches unity (Figs. 4(c), 4(f), and 4(i)). Notably, the Z values of the 5 wt.% MXene/LM/Ni sample are closest to 1, demonstrating its superior impedance matching

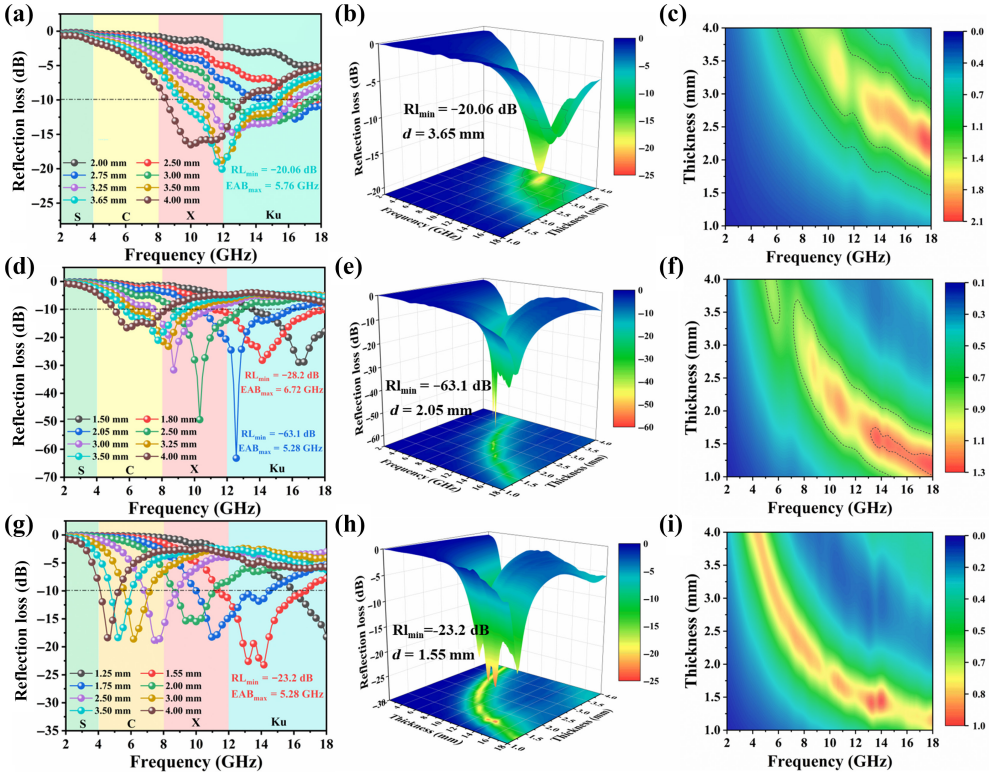

Figure 4 Microwave absorption properties of MXene/LM/Ni composites. RL versus thickness plots, 3D RL plots, and impedance matching of (a)–(c) 3 wt.% MXene/LM/Ni, (d)–(f) 5 wt.% MXene/LM/Ni, and (g)–(i) 8 wt.% MXene/LM/Ni.

characteristics. Consequently, the optimal combination of robust attenuation capacity and excellent impedance matching endows the 5 wt.% composite with exceptional MA performance, characterized by broader bandwidth and stronger absorption intensity (Fig. S8(b) in the ESM). Furthermore, its MA performance surpasses that of most previously reported similar composite materials (Fig. S8(c) and Table S1 in the ESM).

Based on the aforementioned discussions, the EM wave absorption mechanisms of the MXene/LM/Ni composite are proposed and schematically illustrated in Fig. 5(a). Firstly, the amorphous Ga_2O_3 skin on the LM surface serves as a dielectric modulator by suppressing excessive intrinsic conductivity [49, 50]. Simultaneously, the magneto-dielectric synergy among MXene, LM, and Ni chains optimizes the impedance matching characteristic [51, 52]. Secondly, the abundant heterojunctions established between 0D LM, 1D Ni, and 2D MXene trigger intense polarization relaxation via the Maxwell-Wagner-Sillars effect, significantly boosting energy attenuation in the high-frequency THz regime [53–55]. Furthermore, the highly ordered lamellar architecture promotes multiple reflections and scattering of EM waves between heterogeneous layers, effectively extending the propagation path and triggering phase cancellation effects [56–58]. Finally, the robust conductive loss provided by the high carrier mobility of 2D MXene, coupled with the natural resonance of 1D Ni chains and the intense interfacial polarization of LM, collectively enhances EM energy capture and conversion [59–64]. The orchestration of these synergistic mechanisms endows the MXene/LM/Ni composite with exceptional microwave absorption performance.

To evaluate the practical viability of the MXene/LM/Ni composites, RCS simulations were conducted to analyze their far-field microwave absorption performance. Considering that metallic components of military assets generate intense EM scattering, making them susceptible to radar detection, coating these surfaces with microwave absorbing materials (MAMs) is a primary strategy for RCS reduction [65]. For comparative analysis, we investigated 100 mm × 100 mm × 0.5 mm perfect electric conductor (PEC) plate and PEC plates coated with MXene/LM/Ni films of varying filler loadings. At a frequency of 12.56 GHz, 3D scattering patterns were obtained under normal incidence (φ = 0°, θ = 0°) to capture full-angle responses (Figs. 5(b)–5(e)). The results indicate that the scattering signals from the MXene/LM/Ni-coated PEC plates are significantly lower than those from the bare PEC substrate, underscoring the superior microwave absorption of the MXene/LM/Ni composites. To further quantify the signal attenuation relative to the PEC plate, the RCS reduction was calculated (Figs. 5(f) and 5(g)). Under normal incidence, the 5 wt.% MXene/LM/Ni sample achieves a remarkable attenuation value of 27.5 dB·m^2, demonstrating its exceptional efficacy in suppressing EM wave reflections in realistic scenarios.

2.3 Ultra-low reflection THz shielding/absorption performance

THz technology represents a pivotal frontier with immense potential in high-speed communications and high-resolution imaging. Consequently, developing THz-compatible protection materials is imperative to counter the emerging EM pollution and detection threats. Following the verification of microwave absorption, Fig. 6 illustrates the THz absorption and shielding performance of MXene/LM and MXene/LM/Ni composite films within the 0.1–1.6 THz range. THz time-domain spectroscopy (THz-TDS, Fig. 6(a)) reveals the transmission and reflection

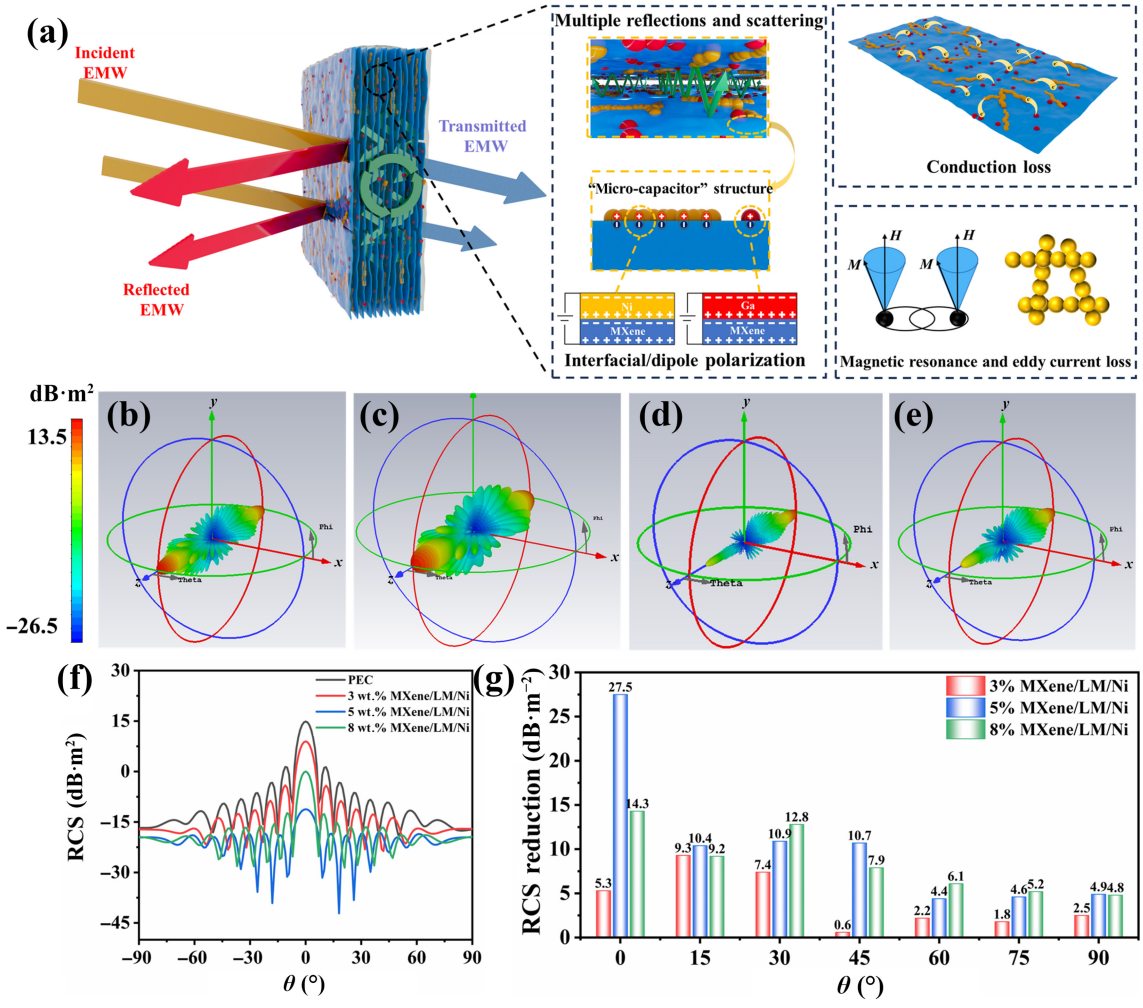

Figure 5 Proposed microwave absorption mechanisms and numerically simulated far-field radar stealth performance of the MXene/LM/Ni composite. (a) Schematic illustration of microwave absorption mechanisms for the MXene/LM/Ni composite film. 3D RCS plots for (b) PEC, PEC substrates covered with (c) 3 wt.% MXene/LM/Ni, (d) 5 wt.% MXene/LM/Ni, and (e) 8 wt.% MXene/LM/Ni. (f) The simulated RCS curves of all samples. (g) RCS reduction values relative to PEC.

profiles of the samples. Compared to the reference signal, both MXene/LM and MXene/LM/Ni films exhibit near-zero transmission signals and transmissivity (Fig. 6(b)). Regarding reflection (Fig. 6(c)), the average reflectivity of MXene/LM/Ni is higher than that of MXene/LM, attributed to the uniform loading of magnetic Ni chains onto the MXene/LM. Correspondingly, the average absorptivity of MXene/LM/Ni is lower than that of MXene/LM (Fig. 6(d)). As shown in Fig. 6(e), the MXene/LM film achieves a maximum SE of 59.9 dB (average 49.8 dB), while the MXene/LM/Ni film reaches a maximum SE of 69.6 dB (average 52.7 dB). Notably, the reflection contribution (SE_R) is less than 3.5 dB (Fig. 6(f)), indicating that the shielding performance is primarily absorption-dominated (Figs. 6(g) and 6(h)). The introduction of Ni chains optimizes impedance matching and constructs more abundant heterojunctions, complex porous channels, and micro-conductive networks, which collectively enhance conductive and polarization losses. Consequently, the MXene/LM/Ni composite stands out as a high-performance THz shielding material characterized by ultra-low reflection (< 3 %) and absorption-dominated extinction. Compared to state-of-the-art materials (Fig. 6(i)), these composite films represent superior candidates for THz protection, effectively realizing microwave-THz compatible defense.

3 Conclusion

In summary, the high-performance MXene/LM/Ni composite films featuring integrated microwave-THz wave protection were successfully fabricated via a combination of electrostatic self-assembly and vacuum-assisted filtration. By strategically orchestrating 0D, 1D, and 2D building blocks within an ordered lamellar architecture, the films achieve an efficient synergy between magneto-dielectric losses and precise impedance matching regulation. Leveraging high-density heterogeneous interface-induced polarization relaxation and interlayer multiple scattering mechanisms, an exceptional microwave-THz compatible protection network is established at an ultra-thin profile. Consequently, the MXene/LM/Ni composite enables multispectral compatible defense across the microwave and THz regimes. Experimental results reveal a record-low RLmin of −63.1 dB at 12.56 GHz and a superior THz SE of 69.6 dB with ultra-low reflectivity (< 5%), leading to a significant reduction in the RCS of the target. This research provides a novel modular paradigm for developing ultra-thin, lightweight, and wideband compatible protection systems, offering robust support for the rapid evolution of advanced stealth technologies and high-frequency communication security applications.

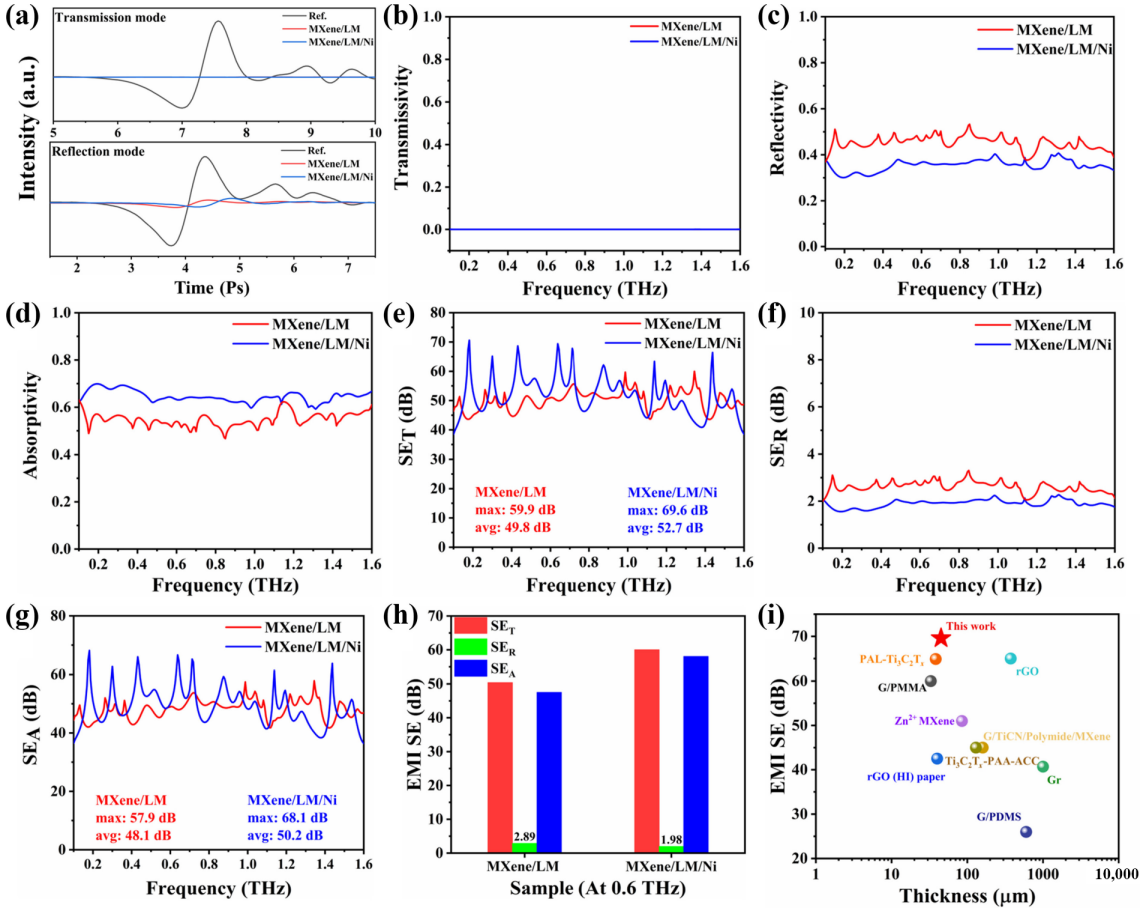

Figure 6 THz wave absorption/shielding performance of MXene/LM and MXene/LM/Ni composite. (a) THz time-domain spectral transmission/reflection signal of MXene/LM and MXene/LM/Ni composite. (b)–(d) Transmission, reflection, and absorption of THz waves for MXene/LM and MXene/LM/Ni composite. (e)–(g) SE_T, SE_R, and SE_A of THz waves for MXene/LM and MXene/LM/Ni composite. (h) The ratio of SE_T, SE_R, and SE_A for MXene/LM and MXene/LM/Ni composite. (i) Comparison of THz wave EMI performance between MXene/LM/Ni composite and other materials. See references in Table S2 in the ESM.

4 Experimental section

4.1 Materials

Hydrochloric acid (HCl, 37%), nickel chloride hexahydrate ($NiCl_2·6H_2O$), ethylene glycol (EG), ethanol, sodium hydroxide (NaOH), liquid metal Ga, and hydrazine hydrate ($N_2H_4·H_2O$, 85%) were purchased from Sinopharm Chemical Reagent Co., Ltd. (China). Ti_3AlC_2 MAX phase (400 mesh) was provided by 11 Technology Co., Ltd. (China). Lithium fluoride (LiF) was obtained from Aladdin Reagent Co. Ltd.

4.2 Synthesis of $Ti_3C_2T_x$ MXene

Few-layer $Ti_3C_2T_x$ MXene nanosheets were synthesized via the minimally intensive layer delamination method. Typically, 2 g of LiF was dissolved in 40 mL of 9 M HCl in a 100 mL Teflon beaker and stirred for 20 min to ensure complete dissolution. Subsequently, 2 g of Ti_3AlC_2 MAX phase powder was gradually introduced into the etchant. The reaction was maintained at 35 °C for 24 h under continuous magnetic stirring to selectively etch the Al layers. The resulting acidic suspension was washed repeatedly with deionized water through centrifugation 3500 rpm, 5 min per cycle) until the supernatant reached a pH value of approximately 6. To achieve delamination, the sediment was redispersed in DI water and subjected to probe ultrasonication for 1 h. Finally, the dispersion was centrifuged at 3500 rpm for 30 min to remove unexfoliated particles. The dark-green supernatant containing few-layer $Ti_3C_2T_x$ nanosheets was collected and freeze-dried for 48 h for further characterization.

4.3 Preparation of LM nanoparticles

Gallium nanoparticles were synthesized via a facile probe ultrasonication method. Typically, 500 mg of bulk LM was introduced into 20 mL of anhydrous ethanol. The mixture was subjected to high-intensity probe ultrasonication (250 W, 40% amplitude) for 30 min in an ice-water bath to prevent excessive thermal oxidation and coalescence of the nanodroplets. During this process, the bulk LM was comminuted into spherical nanodroplets, stabilized by the spontaneously formed native Ga_2O_3 skin. To achieve a uniform size distribution, the resulting suspension was centrifuged at 2000 rpm for 10 min to eliminate larger unfragmented droplets. The gray supernatant containing the LM nanoparticles was collected and stored under an argon atmosphere for further use.

4.4 Synthesis and PDDA functionalization of 1D Ni chains

1D Ni chains were synthesized via a magnetic-field-assisted chemical reduction method. In a typical procedure, 0.5 g of $NiCl_2·6H_2O$ was dissolved in 50 mL of ethylene glycol. The pH of

the solution was adjusted to 12.0 by the dropwise addition of NaOH (2 M in EG). Subsequently, 5 mL of hydrazine hydrate (85 wt.%) was introduced as the reducing agent. The mixture was transferred to a reaction vessel placed between two parallel NdFeB permanent magnets (magnetic field strength approx 200 mT) and maintained at 80 °C for 2 h. The magnetic field directed the growth of Ni nanoparticles into high-aspect-ratio 1D chains. After the reaction, the Ni chains were harvested by a magnet, washed with ethanol and DI water. To facilitate surface modification, the as-prepared Ni chains were dispersed in 50 mL of PDDA aqueous solution (2 wt.%, containing 0.5 M NaCl) and stirred for 12 h. The cationic PDDA molecules were spontaneously adsorbed onto the Ni surfaces through electrostatic interactions. Finally, the PDDA-modified Ni (Ni@PDDA) chains were washed repeatedly to remove excess polymer and redispersed in DI water for subsequent assembly.

4.5 Fabrication of MXene/LM/Ni composite films

The MXene/LM/Ni composite films were fabricated via a controlled electrostatic self-assembly process followed by vacuum-assisted filtration (VAF). Typically, a calculated amount of negatively charged few-layer $Ti_3C_2T_x$ MXene dispersion (2 mg/mL) and LM nanoparticles (2 mg/mL) were first mixed under mild sonication to form a stable MXene/LM hybrid suspension. Subsequently, a specific volume of positively charged PDDA-modified Ni chain (Ni@PDDA) dispersion was added dropwise into the MXene/LM mixture under vigorous stirring. The electrostatic attraction between the cationic Ni@PDDA and the anionic MXene/LM components triggered the formation of a homogeneous hetero-flocculated precursor. The weight ratio of MXene、 LM to Ni chains was precisely adjusted (8:4:1) to optimize the EM performance. The obtained MXene/LM/Ni composite was mixed with paraffin at ratios of 3:97, 5:95, and 8:92 and pressed into rings for testing the EM parameters of coaxial rings. Composite materials with different MXene/LM/Ni contents are denoted as *X*% MXene/LM/Ni. The resulting ternary mixture was filtered through a cellulose membrane (0.22 μm pore size) under vacuum. The obtained wet films were washed with DI water to remove residual ions, dried in a vacuum oven at 40 °C for 12 h, and finally peeled off to MXene/LM and MXene/LM/Ni composite films with a controlled thickness.

4.6 Characterization

The microscopic morphology and structure were observed using transmission electron microscopy (TEM, FEI Tecnai G2 F20) and scanning electron microscopy (SEM, Zeiss Sigma 300). The crystal structure was identified through XRD (Bruker D8 Advance XRD) with Cu Kα radiation (λ = 0.154 nm). The chemical structure was characterized via FTIR (FT-IR, Nicolet 6700) and XPS (Thermo Scientific ESCALAB 250Xi). The magnetic property was measured via a vibrating sample magnetometer (VSM, 7404, LakeShore). The coaxial method was used to measure the EM parameters. The obtained samples were completely immersed in liquid paraffin in a vacuum oven at 80 °C until the pores of the sample were filled with paraffin. After cooling and solidifying, the samples were cut into concentric rings (ϕ_{in} = 3.04 mm, ϕ_{out} = 7.00 mm) for measurement. The RCS performance of the samples was evaluated by CST software to assess their practical application potential. Additionally, the THz shielding performance was experimentally evaluated via a THz time-domain spectroscopy (THz–TDS) system operated in both transmission and reflection modes at room temperature.

Electronic Supplementary Material: Supplementary material (Experimental section, formulas, and additional figures and tables) is available in the online version of this article at https://doi.org/10.26599/NR.2026.94908596.

Data availability

All data needed to support the conclusions in the paper are presented in the manuscript and the Electronic Supplementary Material. Additional data related to this paper may be requested from the corresponding author upon request.

Acknowledgements

This work was financially supported by the 78th batch of grants from the China Postdoctoral Science Foundation (No. 2025M780465), the National Natural Science Foundation of China (No. 52502078), and the key research project of Henan Provincial Higher Education Institutions (No. 26A430034). The authors would like to thank Gang Li from shiyanjia Lab (www.shiyanjia.com) for test of XPS and TEM.

Declaration of competing interest

The authors declare that they have no known competing financial interests or personal relationships that could have appeared to influence the work reported in this paper.

Author contribution statement

H. R. C.: Experimental design, investigation, validation, formal analysis, writing manuscript. J. J. L: Investigation. X. K. J.: Investigation, experimental design, formal analysis. Y. D. Y.: Formal analysis investigation. M. C.: Project administration, investigation. B. B. F.: Project administration, funding acquisition, formal analysis, writing – review & editing. All the authors have approved the final manuscript.

Use of AI statement

None.

References

[1] Wang, L.; Dai, J. Y.; Ding, K. S.; Zeng, H. X.; Cheng, Q.; Yang, Z. Q.; Zhang, Y. X.; Cui, T. J. High-order direct modulation terahertz communications with a wideband time-coding metachip modulator. *Sci. Adv.* **2024**, *10*, eadq8693.

[2] Bai, P.; Zhang, Y. H.; Wang, T. M.; Fu, Z. L.; Shao, D. X.; Li, Z. P.; Wan, W. J.; Li, H.; Cao, J. C.; Guo, X. G. et al. Broadband THz to NIR up-converter for photon-type THz imaging. *Nat. Commun.* **2019**, *10*, 3513.

[3] Kumar, A.; Gupta, M.; Pitchappa, P.; Wang, N.; Szriftgiser, P.; Ducournau, G.; Singh, R. Phototunable chip-scale topological photonics: 160 Gbps waveguide and demultiplexer for THz 6G communication. *Nat. Commun.* **2022**, *13*, 5404.

[4] Akyildiz, I. F.; Jornet, J. M.; Han, C. Terahertz band: Next frontier for wireless communications. *Phys. Commun.* **2014**, *12*, 16–32.

[5] Rappaport, T. S.; Xing, Y. C.; Kanhere, O.; Ju, S. H.; Madanayake, A.; Mandal, S.; Alkhateeb, A.; Trichopoulos, G. C. Wireless communications and applications above 100 GHz: Opportunities and challenges for 6G and beyond. *IEEE Access* **2019**, *7*, 78729–78757.

[6] Liu, R. D.; He, Y. L.; Yang, S. K.; Wang, Q.; Wu, H. J.; Yi, X.

Integration of impedance-gradient and oriented alignment structure in carbon fiber composites enabling thermal management and microwave absorption. *Nano Res.* **2025**, *18*, 94908025.

[7] Xing, L. L.; Cheng, H. R.; Li, Y.; Chen, Q.; Liu, C. T.; Shen, C. Y.; Liu, X. H. MoS_2 decorated on 1D MoS_2@Co/NC@CF Hierarchical fibrous membranes for enhanced microwave absorption. *Small* **2025**, *21*, 2407337.

[8] Gu, W. H.; Tan, J. W.; Chen, J. B.; Zhang, Z.; Zhao, Y.; Yu, J. W.; Ji, G. B. Multifunctional bulk hybrid foam for infrared stealth, thermal insulation, and microwave absorption. *ACS Appl. Mater. Interfaces* **2020**, *12*, 28727–28737.

[9] Cheng, H. R.; Pan, Y. M.; Li, W.; Liu, C. T.; Shen, C. Y.; Liu, X. H.; Pan, C. F. Facile design of multifunctional melamine foam with Ni-anchored reduced graphene oxide/MXene as highly efficient microwave absorber. *Nano Today* **2023**, *52*, 101958.

[10] Li, G. H.; Ma, S. P.; Li, Z.; Zhang, Y. W.; Fan, F.; Huang, Y. Trans-electromagnetic and optical, multi-spectrum compatible defense of $Ti_3C_2T_x$/RGO/ZIF-67(Co) composite aerogel. *Adv. Funct. Mater.* **2025**, *35*, 2423269.

[11] Guan, S. T.; Zhao, Y.; Wei, W. Q.; Ren, H. D.; Yan, Y. X.; Wu, X. L. Rapid synergistic multi-polarization losses enable efficient micro-/terahertz-wave absorption and shielding in WO_3-based 1T/2H-$MoSe_2$ in-plane heterojunctions. *Nano Res.* **2025**, *18*, 94907720.

[12] Wang, B. X.; Xu, W.; Wu, Y. K.; Yang, Z. C.; Lai, S. X.; Lu, L. M. Realization of a multi-band terahertz metamaterial absorber using two identical split rings having opposite opening directions connected by a rectangular patch. *Nanoscale Adv.* **2022**, *4*, 1359–1367.

[13] An, Z. M.; Li, Y. P.; Luo, X. G.; Huang, Y. X.; Zhang, R. B.; Fang, D. N. Multilaminate metastructure for high-temperature radar-infrared bi-stealth: Topological optimization and near-room-temperature synthesis. *Matter* **2022**, *5*, 1937–1952.

[14] Wen, C. Y.; Zhao, B.; Liu, Y. H.; Xu, C. Y.; Wu, Y. Y.; Cheng, Y. F.; Liu, J. W.; Liu, Y. X.; Yang, Y. X.; Pan, H. G. et al. Flexible MXene-based composite films for multi-spectra defense in radar, infrared and visible light bands. *Adv. Funct. Mater.* **2023**, *33*, 2214223.

[15] Ma, W. L.; Liu, X. Y.; Yang, T. Y.; Wang, J. B.; Qiu, Z. R.; Cai, Z. H.; Bai, P. J.; Ji, X. Y.; Huang, Y. Strong magnetic-dielectric synergistic gradient metamaterials for boosting superior multispectral ultra-broadband absorption with low-frequency compatibility. *Adv. Funct. Mater.* **2025**, *35*, 2314046.

[16] Zhu, R. X.; Zhu, H. Z.; Qin, B.; Yao, W. Z.; Zhao, M.; Yu, N.; Su, Z. X.; Xie, L. J.; Ma, H. B.; Huangfu, J. T. et al. Digital camouflage encompassing optical hyperspectra and thermal infrared-terahertz-microwave tri-bands. *Nat. Commun.* **2025**, *16*, 8112.

[17] Wang, H. Y.; Hu, P. F.; Sun, X. B.; Hou, Z. L.; Zhao, P. Y.; Zhou, L.; Yang, S. H.; Geng, C. Y.; Zhu, Y. F.; Wu, X. J. et al. Bioinspired disordered aerogel for omnidirectional terahertz response. *Adv. Mater.* **2025**, *37*, 2418889.

[18] Cheng, Y. J.; Sun, X. X.; Yang, S.; Wang, D.; Liang, L.; Wang, S. S.; Ning, Y. H.; Yin, W. L.; Li, Y. B. Multifunctional elastic rGO hybrid aerogels for microwave absorption, infrared stealth and heat insulation. *Chem. Eng. J.* **2023**, *452*, 139376.

[19] Peng, H. L.; Cai, B.; Zhang, Y.; Gao, L. C.; Zhao, P. Y.; Zhou, L.; Zhang, S.; Liang, W. H.; Xuan, Q. F.; Koo, M. C. et al. Radar-terahertz-infrared compatible stealth coaxial silver nanowire@carbon nano-cable aerogel. *Angew. Chem., Int. Ed.* **2025**, *64*, e202421090.

[20] Cheng, H. R.; Pan, Y. M.; Wang, X.; Liu, C. T.; Shen, C. Y.; Schubert, D. W.; Guo, Z. H.; Liu, X. H. Ni flower/MXene-melamine foam derived 3D magnetic/conductive networks for ultra-efficient microwave absorption and infrared stealth. *Nano-Micro Lett.* **2022**, *14*, 63.

[21] Zhao, T.; Xie, P. Y.; Wan, H. J.; Ding, T. P.; Liu, M. Q.; Xie, J. L.; Li, E. N.; Chen, X. Q.; Wang, T. W.; Zhang, Q. et al. Ultrathin MXene assemblies approach the intrinsic absorption limit in the 0.5-10 THz band. *Nat. Photonics* **2023**, *17*, 622–628.

[22] Yang, S. D.; Lin, Z. Q.; Wang, X. M.; Huang, J. H.; Yang, R. L.; Chen, Z. B.; Jia, Y.; Zeng, Z. P.; Cao, Z. L.; Zhu, H. J. et al. Stretchable, transparent, and ultra-broadband terahertz shielding thin films based on wrinkled MXene architectures. *Nano-Micro Lett.* **2024**, *16*, 165.

[23] Wang, S. N.; Cheng, Z. Y.; Yan, Y.; Yao, J. R.; Liu, Y. J.; Tao, J. Q.; Duan, L.; Weng, Y. L.; Zhu, H. B.; Zhuang, H. Y. et al. Programmable electromagnetic switching in shape-memory-driven liquid metal/polyimide/aramid nanofiber aerogels for intelligent wave management. *Adv. Funct. Mater.*, in press, DOI: 10.1002/adfm.202521612.

[24] Liao, S. Y.; Wang, X. Y.; Li, X. M.; Wan, Y. J.; Zhao, T.; Hu, Y. G.; Zhu, P. L.; Sun, R.; Wong, C. P. Flexible liquid metal/cellulose nanofiber composites film with excellent thermal reliability for highly efficient and broadband EMI shielding. *Chem. Eng. J.* **2021**, *422*, 129962.

[25] Liang, L. Y.; Li, Q. M.; Yan, X.; Feng, Y. Z.; Wang, Y. M.; Zhang, H. B.; Zhou, X. P.; Liu, C. T.; Shen, C. Y.; Xie, X. L. Multifunctional magnetic $Ti_3C_2T_x$ MXene/graphene aerogel with superior electromagnetic wave absorption performance. *ACS Nano* **2021**, *15*, 6622–6632.

[26] Huan, X. H.; Wang, H. T.; Deng, W. C., Yan, J. Q.; Xu, K.; Geng, H. B.; Guo, X. D.; Jia, X. L.; Zhou, J. S.; Yang, X. P. Integrating multi-heterointerfaces in a 1D@2D@1D hierarchical structure via autocatalytic pyrolysis for ultra-efficient microwave absorption performance. *Small* **2022**, *18*, 2105411.

[27] Wang, X. Y.; Lv, X. W.; Liu, Z. W.; Zhang, H. B.; Liu, M. M.; Xu, C. Y.; Zhou, X. D.; Yuan, M. Y.; Yang, L. T.; You, W. B. et al. Multi-interfacial 1D magnetic ferrite@C fibers for broadband microwave absorption. *Mater. Today Phys.* **2023**, *35*, 101140.

[28] Liang, L. Y.; Yao, C.; Yan, X.; Feng, Y. Z.; Hao, X.; Zhou, B.; Wang, Y. M.; Ma, J. M.; Liu, C. T.; Shen, C. Y. High-efficiency electromagnetic interference shielding capability of magnetic $Ti_3C_2T_x$ MXene/CNT composite film. *J. Mater. Chem. A* **2021**, *9*, 24560–24570.

[29] Li, X.; Wu, Z. C.; You, W. B.; Yang, L. T.; Che, R. C. Self-assembly MXene-rGO/CoNi film with massive continuous heterointerfaces and enhanced magnetic coupling for superior microwave absorber. *Nano-Micro Lett.* **2022**, *14*, 73.

[30] Guo, Y. Y.; Chen, Z. Q.; Jin, Z. M.; Wang, X. F.; Zhang, C.; Balakin, A. V.; Shkurinov, A. P.; Peng, Y.; Zhu, Y. M.; Zhuang, S. L. Dynamically controllable terahertz electromagnetic interference shielding by small polaron responses in Dirac semimetal $PdTe_2$ thin films. *Adv. Funct. Mater.* **2024**, *34*, 2407749.

[31] Jiang, H. J.; Yuan, B.; Guo, H. T.; Pan, F.; Meng, F. M.; Wu, Y. P.; Wang, X.; Ruan, L. Y.; Zheng, S. H.; Yang, Y. et al. Malleable, printable, bondable, and highly conductive MXene/liquid metal plasticine with improved wettability. *Nat. Commun.* **2024**, *15*, 6138.

[32] Pan, F.; Rao, Y. P.; Batalu, D.; Cai, L.; Dong, Y. Y.; Zhu, X. J.; Shi, Y. Y.; Shi, Z.; Liu, Y. W.; Lu, W. Macroscopic electromagnetic cooperative network-enhanced MXene/Ni chains aerogel-based microwave absorber with ultra-low matching thickness. *Nano-Micro Lett.* **2022**, *14*, 140.

[33] Liang, L. Y.; Han, G. J.; Li, Y.; Zhao, B.; Zhou, B.; Feng, Y. Z.; Ma, J. M.; Wang, Y. M.; Zhang, R.; Liu, C. T. Promising $Ti_3C_2T_x$ MXene/Ni chain hybrid with excellent electromagnetic wave absorption and shielding capacity. *ACS Appl. Mater. Interfaces* **2019**, *11*, 25399–25409.

[34] Wan, S. J.; Li, X.; Chen, Y.; Liu, N. N.; Du, Y.; Dou, S. X.; Jiang, L.; Cheng, Q. F. High-strength scalable MXene films through bridging-induced densification. *Science* **2021**, *374*, 96–99.

[35] VahidMohammadi, A.; Rosen, J.; Gogotsi, Y. The world of two-dimensional carbides and nitrides (MXenes). *Science* **2021**, *372*, eabf1581.

[36] Dai, B. Z.; Zhao, B.; Xie, X.; Su, T. T.; Fan, B. B.; Zhang, R.; Yang, R. Novel two-dimensional $Ti_3C_2T_x$ MXenes/nano-carbon sphere hybrids for high-performance microwave absorption. *J. Mater. Chem. C* **2018**, *6*, 5690–5697.

[37] Li, J.; He, L. L.; Xia, W. M.; Du, C.; He, L.; Li, X.; You, C. Y.; Zhou,

D. Constructing heterogeneous interfaces of $Ti_3C_2T_x$ MXene magnetic nanocomposites for efficient low-frequency microwave absorption performance. *Carbon* **2025**, *245*, 120786.
[38] Liu, D. W.; Du, Y. C.; Li, Z. N.; Wang, Y. H.; Xu, P.; Zhao, H. H.; Wang, F. Y.; Li, C. L.; Han, X. J. Facile synthesis of 3D flower-like Ni microspheres with enhanced microwave absorption properties. *J. Mater. Chem. C* **2018**, *6*, 9615–9623.
[39] Peng, Y. N.; Meng, X. W.; Wei, H. T.; Tao, L. T.; Wei, Z. X.; Sun, Q.; Zhao, S. L. Controllable construction of hollow Ni/NiO@PPy particles for broadband and highly efficient microwave absorption. *Adv. Funct. Mater.* **2025**, *35*, 2423405.
[40] Parker, T.; Zhang, D. Z.; Bugallo, D.; Shevchuk, K.; Downes, M.; Valurouthu, G.; Inman, A.; Chacon, B.; Zhang, T.; Shuck, C. E. et al. Fourier-transform infrared spectral library of MXenes. *Chem. Mater.* **2024**, *36*, 8437–8446.
[41] Yi, P.; Zou, H. H.; Yu, Y. H.; Li, X. F.; Li, Z. Y.; Deng, G.; Chen, C. Y.; Fang, M.; He, J. Z.; Sun, X. et al. MXene-reinforced liquid metal/polymer fibers via interface engineering for wearable multifunctional textiles. *ACS Nano* **2022**, *16*, 14490–14502.
[42] Cui, Y. H.; Liu, Z. H.; Zhang, Y. F.; Liu, P.; Ahmad, M.; Zhang, Q. Y.; Zhang, B. L. Wrinkled three-dimensional porous MXene/Ni composite microspheres for efficient broadband microwave absorption. *Carbon* **2021**, *181*, 58–68.
[43] Luo, W.; Wang, M. Y.; Wang, K. J.; Yan, P.; Huang, J. L.; Gao, J.; Zhao, T.; Ding, Q.; Qiu, P. P.; Wang, H. F. et al. A robust hierarchical MXene/Ni/aluminosilicate glass composite for high-performance microwave absorption. *Adv. Sci.* **2022**, *9*, 2104163.
[44] Wang, W. Z.; Wang, J. F.; Cheng, H. R.; Chen, Q.; Liu, X. H. Polypyrrole decorated 3D hierarchical heterostructured CoNi/NC@melamine foam for enhanced microwave absorption. *Chem. Eng. J.* **2025**, *523*, 168576.
[45] Yang, P. A.; Wang, L.; Ruan, H. B.; Deng, W. J.; Li, R.; Shou, M. J.; Huang, X.; Zhang, Y. X.; Lu, Y. Heterogeneous interface engineering and directional tuning electromagnetic parameters of MXene/Fe NPs absorbers for precise low-frequency microwave absorption. *Nano Res.* **2025**, *18*, 94907783.
[46] Qu, N.; Xu, G. X.; Liu, Y. K.; He, M. K.; Xing, R. Z.; Gu, J. W.; Kong, J. Multi-scale design of metal-organic framework metamaterials for broad-band microwave absorption. *Adv. Funct. Mater.* **2025**, *35*, 2402923.
[47] Chen, P.; He, S. B.; Zou, Z. K.; Wang, T. Y.; Hu, J. F.; Tao, J. R.; Yang, L.; Li, Y. W. Intelligent hydrogels enabled large-scale variability in continuously tunable microwave absorption. *Adv. Funct. Mater.* **2025**, *35*, 2506308.
[48] Tian, H. H.; Guo, Q. F.; Liu, S. C.; Jiao, K.; Ren, X. G.; Liu, J. Y.; Hao, H.; Yin, J. B.; Long, J.; Wang, Y. et al. Robust single-walled carbon nanotube-coated aramid fibers with tunable conductivities for broadband radar absorption in honeycomb structures. *ACS Nano* **2025**, *19*, 21729–21738.
[49] Zhao, K. Y.; Luo, C. L.; Sun, C.; Huang, M. L.; Wang, M. Construction of heterogeneous interfaces on Ti_3AlC_2 micro-particles via surface dotting liquid metal to enhance electromagnetic wave absorption performance. *Compos. Part A: Appl. Sci. Manuf.* **2023**, *173*, 107640.
[50] Zhao, B.; Du, Y. Q.; Lv, H. L.; Yan, Z. K.; Jian, H.; Chen, G. Y.; Wu, Y. Y.; Fan, B. B.; Zhang, J. C.; Wu, L. M. et al. Liquid-metal-assisted programmed galvanic engineering of core-shell nanohybrids for microwave absorption. *Adv. Funct. Mater.* **2023**, *33*, 2302172.
[51] Zhao, B.; Yan, Z. K.; Liu, L. L.; Zhang, Y. Y.; Guan, L.; Guo, X. Q.; Li, R. S.; Che, R. C.; Zhang, R. A liquid-metal-assisted competitive galvanic reaction strategy toward indium/oxide core-shell nanoparticles with enhanced microwave absorption. *Adv. Funct. Mater.* **2024**, *34*, 2314008.
[52] Wang, J. Q.; Wu, Z.; Xing, Y. Q.; Liu, L. A novel 1D/2D interpenetrating network architecture of MXene/cellulose composite microfiber and graphene for broadband microwave absorption. *Chem. Eng. J.* **2022**, *439*, 135734.
[53] Liu, X. Y.; Ma, W. L.; Yang, T. Y.; Qiu, Z. R.; Wang, J. B.; Li, Y. H.; Wang, Y.; Huang, Y. Multilevel heterogeneous interfaces enhanced polarization loss of 3D-printed graphene/$NiCoO_2$/selenides aerogels for boosting electromagnetic energy dissipation. *ACS Nano* **2024**, *18*, 10184–10195.
[54] Ma, S. P.; Li, G. H.; Li, Z.; Wang, T. Y.; Zhang, Y. W.; Li, N. N.; Chen, H. S.; Zhang, N.; Liu, W. W.; Huang, Y. Negative photoconductivity of Fe_3GeTe_2 crystal with native heterostructure for ultraviolet to terahertz ultra-broadband photodetection. *Adv. Mater.* **2024**, *36*, 2305709.
[55] Ma, S. P.; Li, G. H.; Li, Z.; Zhang, Y. W.; Lu, H. L.; Gao, Z. S.; Wu, J. X.; Long, G. K.; Huang, Y. 2D magnetic semiconductor Fe_3GeTe_2 with few and single layers with a greatly enhanced intrinsic exchange bias by liquid-phase exfoliation. *ACS Nano* **2022**, *16*, 19439–19450.
[56] Fan, B. B.; Zeng, X. J.; Fan, X. M.; Huang, X. X. Editorial for the special issue on frontiers in advanced ceramic materials for microwave absorption. *J. Adv. Ceram.* **2025**, *14*, 9221215.
[57] Li, M. R.; Zhao, K. Y.; Fan, B. B.; Li, Y.; Tan, D. L.; Wang, H. L.; Gao, Q. L.; Li, W.; Zhang, H. S.; Zhu, Y. Q. et al. Rational a-site entropy engineering in perovskites: Dual-exchange enhanced magnetoelectric coupling for ultra-efficient microwave absorption. *Adv. Sci.* **2026**, *13*, e16938.
[58] Li, M. R.; Li, W.; Wang, Y. X.; Sun, F.; Wang, Q.; Tan, D. L.; Zhang, R.; Wang, H. L.; Shao, G.; Liu, Y. L. et al. Entropy-driven microwave absorption enhancement in hexagonal $(Ba_{1/3}Sr_{1/3}Ca_{1/3})FeO_3$ perovskite. *J. Adv. Ceram.* **2025**, *14*, 9221059.
[59] Zha, L. L.; Wei, C. Y.; Liu, J. J.; Yang, Y.; Wu, B.; Zhang, X. H.; Wu, J. H. The core-shell structure of nitrogen-doped carbon coated Fe_3O_4 decorated MXene for broadband and efficient microwave absorption. *Ceram. Int.* **2024**, *50*, 5453–5463.
[60] Zha, L. L.; Zhang, X. H.; Wu, J. H.; Liu, J. J.; Lan, J. F.; Yang, Y.; Wu, B. Enhanced electromagnetic wave absorption based on $Ti_3C_2T_x$ loaded nickel nanoparticles via polydopamine connection. *Ceram. Int.* **2023**, *49*, 20672–20681.
[61] Zhang, X. H.; Wei, C. Y.; Zha, L. L.; Chen, J. W.; Wang, J. W.; Yu, H. L.; Wu, J. H. Facile one-pot synthesis of polypyrrole-coated magnetic montmorillonite for enhanced microwave absorption and sunlight-induced heat generation. *J. Alloys Compd.* **2024**, *971*, 172676.
[62] Liang, H. S.; Guo, Y. L.; Hui, S. C.; Hou, Z. Y.; Wang, Z.; Shen, H.; Wu, H. J. Tailoring dielectric-magnetic synergy in bimetallic MOF-derived Cu/C@Fe_3O_4 for high-efficiency electromagnetic wave absorption. *Carbon* **2025**, *243*, 120605.
[63] Liang, H. S.; Hou, T.; Liu, T. C.; Hui, S. C.; Hou, Z. Y.; Wang, Z.; Shi, B.; Zhang, L. M.; Shen, H.; Wu, H. J. Rare-earth oxide-induced interfacial engineering for tailoring dielectric response in $NiCo_2O_4$/CeO_2 composites toward high-performance electromagnetic wave absorbers. *Carbon* **2026**, *246*, 120922.
[64] Wen, J. M.; Liu, Y. Y.; Hui, S. C.; Deng, L. C.; Zhang, L. M.; Fan, X. M.; Chen, Q.; Liu, X. M.; Li, X. C.; Yan, N. et al. Lattice compressive strain-controlled electromagnetic wave absorption in TMDs by plasma-assisted rapid annealing. *Matter* **2025**, *8*, 102151.
[65] Jin, K. X.; Li, X. A.; Shi, Y. N.; Wang, C. S.; Guo, W. C.; Tian, K. S.; Wang, H. Y. Defects in discrete nanocrystals of thin-shelled amorphous carbon induced dipole polarization for boosting broadband response. *Adv. Funct. Mater.* **2026**, *36*, e14258.